Front. Earth Sci. 2023, 17(1): 251–261
https://doi.org/10.1007/s11707-022-0989-y

RESEARCH ARTICLE

Insights into lithium adsorption by coal-bearing strata kaolinite

Yu CHEN, Hao ZHAO, Mingzhe XIA (✉), Hongfei CHENG (✉)

School of Earth Science and Resources, Chang'an University, Xi'an 710054, China

Abstract The sharp increase in the demand for lithium (Li) for high-energy-storage battery materials due to its high specific energy and low negative chemical potential render Li a geopolitically significant resource. It is urgent to develop a low-cost, efficient method to improve lithium extraction. Herein, Li ion (Li^+) adsorption in coal-bearing strata kaolinite (CSK) was studied. The effects of pre-activation acid leaching (meta-kaolinite/H_2SO_4, MK-HS) and dimethyl sulfoxide intercalation (coal-bearing strata kaolinite/dimethyl sulfoxide, CSK-DMSO) on the Li^+ adsorption capacity were studied under the same adsorption conditions. The results indicated that the adsorption was completed in 60 min under alkaline conditions (pH = 8.5), a high solution concentration (400 mg/L), and a low dosage (1 g/100 mL); and the comprehensive adsorption capacity is MK-HS > CSK-DMSO > CSK. Furthermore, the DMSO intercalation caused the interlayer spacing of the CSK to increase, which provided more space for Li^+ to enter and increase the adsorption capacity. After thermal pre-activation and acid leaching, structural failure and lattice collapse resulted in the presence of more micropores in the MK-HS, which resulted in a 10-fold increase in its specific surface area and caused coordination bond changes (Al(VI) to Al(IV)) and leaching of aluminum (Al) from the lattice. It is proposed that these structural changes greatly improve the activity of CSK so that Li^+ cannot only adsorb onto the surface and between the layers but can also enter the lattice defects, which results in the MK-HS having the best adsorption performance. Combined with the adsorption kinetics analysis, the adsorption methods of CSK and two modified materials include physical adsorption and chemical adsorption. In this study, the adsorption capacity of CSK and its modified products to Li were explored, providing a new option for the reuse of CSK and the extraction of Li.

Received November 3, 2021; accepted March 16, 2022

E-mail: zymzxia@chd.edu.cn (Mingzhe XIA)
h.cheng@chd.edu.cn (Hongfei CHENG)

Keywords coal-bearing strata kaolinite, lithium, adsorption, modification

1 Introduction

The problems of environmental pollution and energy shortages caused by the development of industrialization urgently need to be solved (Grosjean et al., 2012). Developing environmentally friendly new energy sources has become an urgent demand. As the least dense metal element (ρ = 0.53 g/cm^3 at 20°C), with a strong metal activity, the highest electrochemical potential (3.82 V), and a high specific energy (460–600 Wh/kg) and redox potential, lithium (Li) could be a great energy storage material (Cheng et al., 2021b). In particular, as a key new energy storage technology, the global demand for Li resources has increased significantly with the rapid development of new energy vehicles in recent years. Li mainly exists in the form of solid minerals (e.g., spodumene and lepidolite), brine, and seawater in nature (Harvianto et al., 2016; Razmjou et al., 2019). According to statistics (Liu et al., 2017), Li in salt lake brines accounts for 66% of the total Li resources. The Li reserves in seawater are 2.3 billion tons (Cheng et al., 2021a), which is dozens of times larger than terrestrial Li reserves (~86 million tons). At present, the techniques for extracting Li deposited in liquids mainly include electrochemical processes (Xu et al., 2016; Paranthaman et al., 2017), nanofiltration membrane separation (Xu et al., 2021; Zhao et al., 2021), solvent extraction (Wang et al., 2014; Swain, 2016), and adsorption (Luo et al., 2021). Compared with adsorption methods, electrochemical processes, nanofiltration membrane separation, and solvent extraction have the problems of complicated reaction conditions, high costs, and environmental pollution, respectively (Wang et al., 2021a). Hence, finding a low-cost, high-efficiency, environmentally friendly adsorption material for Li extraction from liquids

is critical.

Coal gangue is a solid waste produced during the process of coal mining and washing, accounting for 10%–15% of total coal production. The accumulation of considerable coal gangue not only occupies a great deal of land, but also results in serious environmental problems (Li and Wang, 2019). It is imperative to investigate the optimum plan of coal gangue utilization and environmental protection. Because of high proportion of kaolinite (Kaol) (50%–98%), coal gangue is also called coal-bearing strata kaolinite (CSK) and has similar physical and chemical properties to Kaol (Tao et al., 2008). Therefore, the application method of Kaol could be applied to CSK. Kaol is widely used in medical, ceramic, chemical, and other industries due to its good heat resistance, plasticity, adsorption, and other properties (Suraj et al., 1998; Uddin, 2017). The weak hydrogen bonds and Vander Waals force between the layers lead to Kaol having a low surface reactivity and easily cracking and slipping (Cheng et al., 2018), which makes the Kaol interlayers available for intercalation and expansion, which increases its specific surface area and improves its adsorption capacity. Experiments on heavy metal ion adsorption onto Kaol have studied the specific adsorption capacity and competitive adsorption effect of Kaol on Pb^{2+}, Cd^{2+}, Ni^{2+}, Cu^{2+}, and other metals in aqueous medium using the control variable method (Gupta and Bhattacharyya, 2005; Bhattacharyya and Gupta, 2006; Bhattacharyya, 2008; Sen Gupta and Bhattacharyya, 2008; Jiang et al., 2010). Furthermore, Kaol has been modified by acid leaching (Jia et al., 2019; Zhou et al., 2021), peeling, intercalation (Cheng et al., 2010, 2012a, 2015), and grafting (Wang et al., 2017; Zhou et al., 2019) to improve its ability to remove metal ions from aqueous medium (Cheng et al., 2021a). Combined with the adsorption performance of Kaol, CSK may be used for the adsorption of Li, and high content of carbonaceous organic matter might result in the better adsorption capacity for Li. It is of great significance to solve the environmental protection problems caused by the treatment of CSK and the extraction of Li.

In this study, CSK was modified through pre-activation acid leaching (meta-kaolinite/H_2SO_4, MK-HS) and DMSO intercalation (coal-bearing strata Kao1/dimethyl sulfoxide, CSK-DMSO) to study its lithium ion (Li^+) adsorption capacity. In addition, the adsorption mechanism was studied based on structure and morphology characterization analysis and its adsorption kinetics.

2 Experiments

2.1 Materials

The CSK used in the experiments was obtained from Xinzhou, Shanxi Province, China. The chemical compositions of CSK are shown in Table 1. The reagents used in this study, namely, Li sulfate monohydrate ($Li_2SO_4·H_2O$), sodium hydroxide (NaOH), sulfuric acid (H_2SO_4), dimethyl sulfoxide (DMSO), and methanol (CH_3OH), were purchased from Shanghai Aladdin Biochemical Technology Co., Ltd. (China). All of the chemical reagents were of pure analytical grade and did not require additional purification or other treatment.

2.2 Preparation of modified Kaol

The powdered CSK was dried for 4 h at 70°C, and DMSO solution with a concentration of 90% was prepared. After drying, the CSK was mixed with the configured DMSO solution (1:5 S/L ratio). Then, the mixture was placed in a water bath thermostatic magnetic mixer at 70°C and was heated and stirred for 24 h. Finally, the CSK-DMSO was made after drying the intercalated CSK and separating it from the solution via filtering.

The preparation of the MK-HS mainly involved two steps: thermal pre-activation and leaching in the H_2SO_4 solution. During the thermal pre-activation process, the CSK was placed in a muffle furnace and calcined at 500°C and 600°C for 4 h to obtain two types of thermally pre-activated meta-kaolinite (MK-500 and MK-600, respectively). During the acid leaching process, the MK-600 was mixed with the prepared H_2SO_4 solution at a mass ratio of 1:2 S/L, and then, it was heated for 4 h at 80°C. Then, the waste liquid was pumped out and the resulting acid modified MK-600 was washed with ultrapure water to remove the acid attached to the surface of the CSK. Finally, the MK-600 leached using H_2SO_4 (MK-HS) was obtained after drying the washed Kaol complex for 6 h at 70°C.

2.3 Characterization

The X-ray diffraction (XRD) patterns of the samples were obtained using an X-ray diffraction instrument with filtered Cu Kα radiation (n = 1.5406 Å) operated at 40 kV and 40 mA (Bruker, Germany). The XRD pattern was recorded from 2.5° to 45°, with a scanning speed of 2° per min. Fourier-transform infrared spectroscopy (FTIR;

Table 1 Chemical compositions of CSK

SiO_2	TiO_2	Al_2O_3	Fe_2O_3	MnO	MgO	CaO	Na_2O	K_2O	P_2O_5	LOI	TOTAL
43.19%	1.22%	37.92%	0.22%	0.01%	0.16%	0.33%	<0.01%	0.41%	0.06%	16.48%	100%

Thermo Scientific Nicolet iS10, China) was used to determine the chemical bonds and functional groups of the samples, and KBr pellets were used as the blank. A scanning electron microscope (SEM; S-4800, Hitachi, Japan) and energy dispersive spectrum analysis (EDS) at 5.0 kV and 20 kV was used to observe the surface morphologies of the samples. The zeta potentials of the samples were acquired using a Malvern Zetasizer Nano ZS90 (UK).

2.4 Adsorption experiments

In this study, except for the specific conditions corresponding to each of the following four influencing factors in the experiments, the other adsorption conditions were the same: a solution concentration of 300 mg/L, a solution volume of 100 mL, a reaction time of 3 h, and a pH value of 6.5. In addition, the amount of additives was 2 g, and the environmental temperature was 25°C. Moreover, a constant temperature bath oscillator was used to ensure that the adsorbent and solution contact and the reaction were more complete. First, to study the adsorption effect for different amounts of absorbent, 1–5 g of the three prepared adsorbents (CSK, CSK-DMSO, and MK-HS) were mixed with a Li solution with a concentration of 300 mg/L. In addition, to investigate the adsorption effects for different pH values, the three adsorbents were reacted with solutions with five different pH values (2.5, 4.5, 6, 6.5, and 8.5). Different solution concentrations (50 mg/L, 100 mg/L, 200 mg/L, 300 mg/L, and 400 mg/L) were set to study the influence of the concentration on the adsorption effect. The adsorption saturation time of each of the three adsorbents was determined by dividing the reaction time of the different conditions (30 min, 60 min, 90 min, 120 min, and 180 min). After each adsorption experiment, the solid was separated from the solution using a filter, and the filtered solution was centrifuged for 10 min at a speed of 5000 r/min. An inductively coupled plasma emission spectrometer (Thermo ICAP 6300) was used to measure the Li^+ concentration of the upper liquid after centrifugation.

To analyze the experimental data, the removal efficiency (P) and adsorption capacity (R_e (mg/g)) of each of the three different adsorbents (CSK, CSK-DMSO, and MK-HS) in the solution were calculated using the following equations:

$$P = \frac{C - C_e}{C} \times 100\%, \tag{1}$$

$$R_e = \frac{(C - C_e)}{\mathrm{m}} \times V, \tag{2}$$

where C_e is the initial concentration of the Li solution, and C is the concentration after adsorption of the Li solution. V and m represent the volume (L) of the Li solution and the mass of the adsorbent (g) used in the Li solution, respectively.

The adsorption dynamics are of great significance in studying the adsorption balance time and mechanism. In this study, the experimental data were fitted with two adsorption dynamics equations, that is, a pseudo-first-order dynamics model and a pseudo-second-order dynamics model, to determine the rate constant and adsorption balance of the adsorption process. The pseudo-first-order kinetic model (Eq. (3)) assumes that the rate of change of the solute adsorption is directly proportional to the difference between the saturated concentration and the adsorbed solid absorption. The pseudo-second-order kinetic model (Eq. (4)) assumes that the adsorption rate is controlled by the chemical adsorption mechanism.

$$\lg(Q_e - Q_t) = \lg Q_e - \frac{k_{ad}}{2.303} \times t, \tag{3}$$

$$\frac{t}{q} = \frac{1}{kQ_e^2} + \frac{1}{Q_e} \times t, \tag{4}$$

where Q_e indicates that the adsorption is in equilibrium; Q_t is the adsorption capacity of the Li^+ at any time t; and k_{ad} and k are the rate constants of the pseudo first-order and pseudo second-order kinetic models, respectively.

3 Results and discussion

3.1 Structural features

The XRD patterns of the CSK, CSK-DMSO, MK-500, MK-600, and MK-HS are presented in Fig. 1(a). The reflection of the CSK is high, narrow, and sharp, which is consistent with the standard card (PDF#78-2109). The peak value is the highest at the characteristic reflection point, with a base spacing of 0.71 nm at an angle of 2θ = 12.36°, indicating the high purity and good crystallization degree of the Kaol. At 2θ = 24.86°, the reflection with a base spacing of 0.35 nm is a secondary diffraction of d (002). According to the Scherre equation, the grain size of the CSK was calculated to be 40.4 nm. However, a new high-intensity diffraction peak appeared in CSK-DMSO at 2θ = 7.86°, increasing the base spacing to 1.12 nm. This demonstrates that the DMSO was successfully intercalated into the interlayer of the Kaol, which increased the spacing between the layers (Cheng et al., 2012b; Cheng et al., 2017).

As shown in Fig. 1(a), there is a large difference in the diffraction alignments for the calcinations at 500°C and 600°C. The reflection of the MK-500 at 2θ = 12.34° is basically the same as that of the CSK, except for a decrease in the diffraction intensity, which demonstrates that the crystal structure of the CSK was not affected. However, the height of the characteristic reflection values in the spectra of MK-600 and MK-HS decreased after

heating for 4 h at 600°C, and the characteristic reflection at 2θ = 12.36° disappeared. The reflection intensity of d (001) in the MK-600 and MK-HS spectra is greatly weakened, and only the quartz reflection peak at 2θ = 26.54° was observed, which indicates that the hydroxyl has been released and the structural hydroxyl in the CSK has started to be dislodged. Although the original layered structure has not been completely destroyed, the structure of the atoms has been offset, and it is no longer stable. Additionally, the CSK changed into amorphous meta-kaolinite after heating at 600°C, and the Al atom in the structure changed from the original stable Al(VI) to unstable Al(IV), at which time the CSK had the highest activity (Peng et al., 2014).

FTIR was used to study the surface functional groups of the CSK, MK-500, MK-600, CSK-DMSO, and MK-HS (Fig. 1(b)). For CSK, the absorption bands at 470 cm^{-1} and 475 cm^{-1} are attributed to Si-O-Si deformation, and the absorption band at 540 cm^{-1} is assigned to the Al-O-Si vibration. Furthermore, the characteristic bands at 693 cm^{-1} and 797 cm^{-1} are due to O-Al-OH translational vibrations and O-Si-O vibrations, respectively (Cao et al., 2021; Zhao et al., 2022). The characteristic bands from 916 cm^{-1} to 937 cm^{-1} are caused by Al-OH bending vibration, while the absorption bands at 1010 cm^{-1} and 1116 cm^{-1} are caused by Si-O-Si deformation. Moreover, the bands at 3623 cm^{-1} and 3691 cm^{-1} are caused by different hydroxyl vibrations. The characteristic band at 3623 cm^{-1} is caused by the stretching of the hydroxyl in the Kaol layer, while the characteristic band at 3691 cm^{-1} is caused by stretching of the hydroxyl on the inner surface of the Kaol layer (Xing et al., 2019).

Compared with the FTIR spectrum of the CSK, the characteristic band of MK-500 is basically the same as that of CSK, which demonstrates that the calcination at 500°C did not have a significant impact on the structure and functional group of the CSK. However, the characteristic absorption band in the FTIR spectrum of MK-600 is greatly reduced. In particular, the absorption bands at 3623–3691 cm^{-1} and 916–937 cm^{-1} disappeared, demonstrating that calcination at 600°C caused the dehydroxylation of the CSK. The absorption bands at 1039 cm^{-1} and 1116 cm^{-1} were widened. These are the characteristic bands caused by amorphous silicon. This verifies that the CSK underwent amorphous changes at 600°C and formed meta-kaolinite (Makó et al., 2016). In addition, the characteristic absorption band in the spectrum of MK-HS at 797 cm^{-1} is caused by the Al(IV)-O bond, indicating that the Al in the layer was converted from Al(VI) to Al(IV) (Makó et al., 2016). It should be noted that the characteristic absorption bands of the CSK-DMSO are similar to those of the CSK in the lower wavenumber range, but new characteristic absorption bands were observed in the higher wavenumber range. The characteristic absorption bands at 1319 cm^{-1} to 1429 cm^{-1} are formed by the bending vibration of CH_3, and the characteristic absorption band at 3022 cm^{-1} is caused by a new form of C-H asymmetrical stretching vibration.

3.2 Morphological features

Figure 2(a) shows a pseudo-hexagonal plate-shaped, two-layered, stacking structure. The crystal surface is smooth, with a diameter of about 0.2–4 μm. After calcination at 600°C, as can be seen from Fig. 2(b), the flaky structure of MK-600 was still retained, but some of the surface melted. Simultaneously, the layered structure became dense and the particles became agminated, which may be conducive to the formation of large holes. Furthermore, the high temperature caused the dehydroxylation in the CSK and the crystal structure to be destroyed, which may be beneficial to increasing the specific surface area. In addition, the morphology of the MK-HS is significantly different from those of the CSK and MK-600 in terms of the uneven distribution of the particles and the large differences in size (Fig. 2(c)). The surface of the

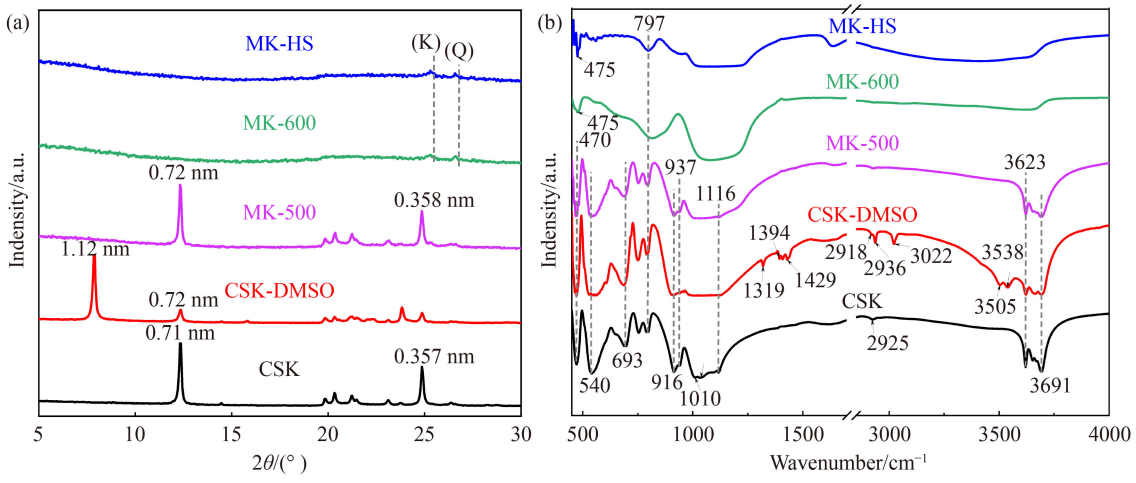

Fig. 1 (a) XRD patterns and (b) FTIR spectra of the CSK, CSK-DMSO, MK-500, MK-600, and MK-HS.

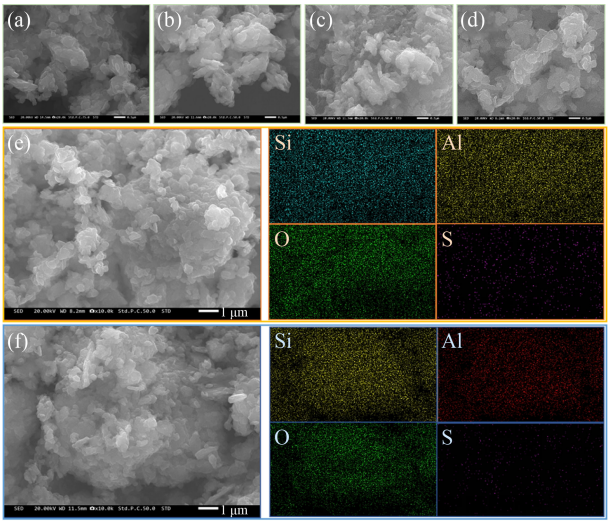

Fig. 2 SEM images of (a) CSK, (b) MK-600, (c) MK-HS, and (d) CSK-DMSO, and EDS patterns of (e) CSK-DMSO and (f) MK-HS.

laminated structure became rough, the stacking mode of the layer was not as regular as that of the CSK, and loose stacking occurred simultaneously. Moreover, the surface area increased, which is theoretically more conducive to adsorption. As is shown in Figs. 2(d) and 2(e), after the DMSO intercalation, it was observed that the size of the crystal particles was very similar to those of the CSK, but the thin layer overlay was reduced due to the increased layer spacing and the overall increase in surface area after the DMSO intercalation. Additionally, Figs. 2(e) and 2(f) show the mapping of the CSK-DMSO and MK-HS, respectively. As is shown in Fig. 2(e), Si, O, and Al were uniformly distributed on the surface of the CSK-DMSO, and S was abundantly distributed on the surface due to the DMSO intercalation. Compared with the CSK-DMSO, the distribution of Al decreased significantly in the MK-HS (Fig. 2(f)), which was caused by the leaching of aluminum by the acid.

Pore size and surface area are the main factors influencing adsorption capacity. In this study, the surface area and pore distribution of the CSK, CSK-DMSO, MK-500, MK-600, and MK-HS were analyzed (Fig. 3 and Table 2). It was found that the isothermal adsorption curves of the CSK, CSK-DMSO, MK-500, and MK-600 significantly conformed to type IV isothermal curves and type H_3 hysteresis loops, which indicates that they all have mesoporous adsorption properties (Wang et al., 2021b; Wang et al., 2022). According to the isothermal adsorption curves of CSK, MK-500, and MK-600, the specific surface area of the CSK gradually decreased with

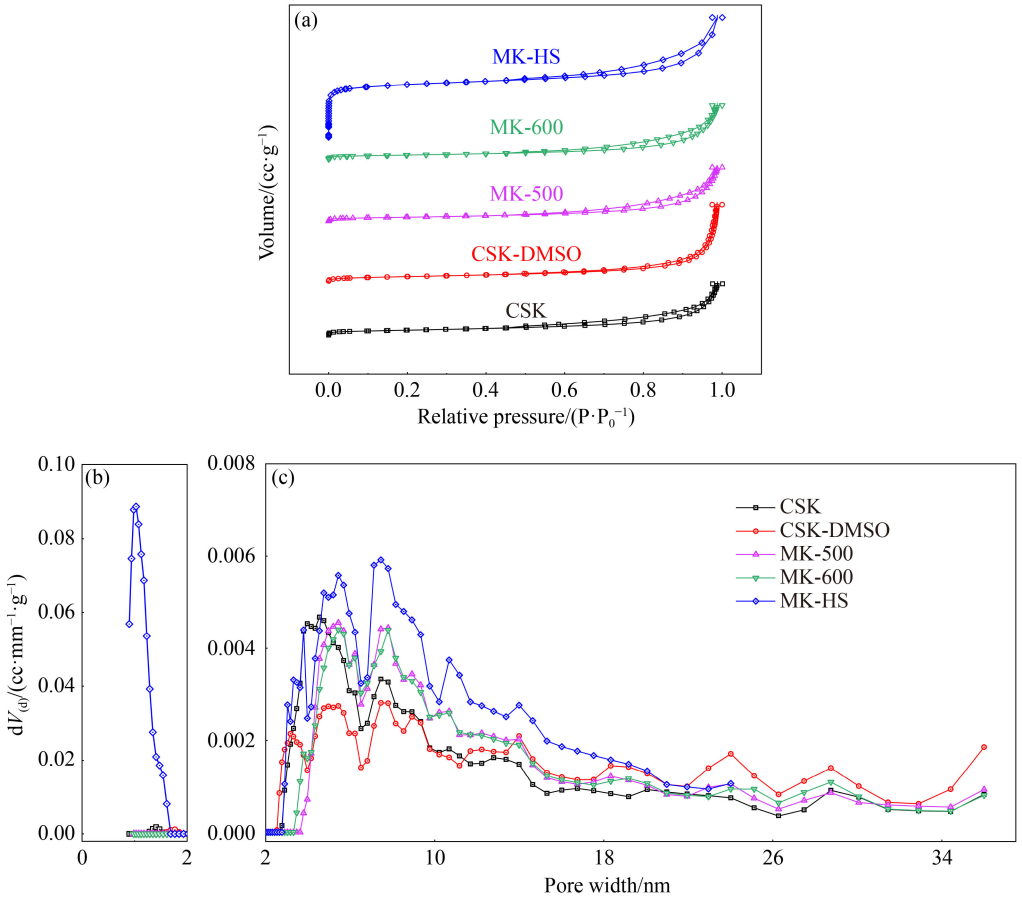

Fig. 3 (a) Nitrogen adsorption-desorption curves, (b) and (c) DFT pore size distribution curves of different adsorbents.

Table 2 Pore structure properties of CSK, CSK-DMSO, MK-500, MK-600 and MK-HS

Samples	SBET/ ($m^2 \cdot g^{-1}$)	Pore volume/ ($cm^3 \cdot g^{-1}$)	Average pore diameter/nm
CSK	14.998	0.045	4.543
CSK-DMSO	13.841	0.050	7.452
MK-500	12.058	0.049	5.439
MK-600	12.516	0.047	5.342
MK-HS	170.404	0.113	1.029

increasing temperature, which was mainly caused by the collapse of some of the structures under the high temperatures. However, the specific surface area of CSK-DMSO is not significantly different from that of CSK, but its average pore size increased to 7.452 nm (Table 2). Thus, it is speculated that the DMSO effectively improved the pore size without damaging the structure of the CSK. Furthermore, the MK-HS exhibits an excellent adsorption effect at relatively low pressures, which demonstrates that not only does the MK-HS have mesoporous adsorption properties, but it also has a large number of micropores. These micropores may be produced by the serious damage to the layered structure caused by the acid leaching, which could rationally explain why the specific surface area of the MK-HS increased to 170 m^3/g. In addition, the pore size distribution of the MK-HS is mainly in the range of 1–2 nm (Fig. 3(b)), which is consistent with the results of the isothermal adsorption curve analysis, indicating that the acid leaching did indeed destroy the lamellar structure of the CSK and caused it to break into small particles. It is discernable that 2–20 nm is the main aperture distribution range of CSK, MK-500, and MK-600 (Fig. 3(c)). However, the average pore size of CSK-DMSO is evenly distributed in the range of 2–30 nm, which may be because the intercalation expanded the pore volume.

Based on the above comparison of the structural characteristics and morphological characteristics, CSK-DMSO and MK-HS exhibit obvious differences compared with CSK. Thus, the following discussion mainly focuses on these three samples.

3.3 Zeta potential features

The surface charge plays an important role in the adsorption performance of the adsorbent. The zeta potential was used to analyze the effects of three Kaol adsorbents (CSK, CSK-DMSO, and MK-HS) on the surface electrical properties at pH values from 1 to 8 (Fig. 4). The zeta potentials of the CSK, CSK-DMSO, and MK-HS decreased with increasing pH, demonstrating the absolute effect of pH on the surface electrical properties of the adsorbents. For the initial low pH value, the negative charge of the three adsorbents was the lowest, and the electrical value of the CSK-DMSO was the closest to 0 mV. All of the adsorbents exhibited weak cation adsorption capacities. As the pH value increased, the rate of decrease of the surface charge of the MK-HS remained relatively stable, varying from −7.72 to −22.47 mV. The minimum value of CSK reached −27.5 mV at pH = 7, and CSK-DMSO had the best negative electronegativity at a pH of 8. According to the univariate linear fitting results, it can be roughly speculated that the effect of pH on the adsorption capacities of the three adsorbents is as follows: the adsorption capacities of these three adsorbents increased with increasing pH.

3.4 Factors influencing adsorption

The effect of the initial concentration on the adsorption of Li^+ by CSK, CSK-DMSO, and MK-HS was examined and is shown in Fig. 5(a). As the Li^+ concentration of the solution increased, the unit adsorption of Li^+ by the three adsorbents gradually increased, indicating that the solution containing higher concentrations of metal ions exhibited a higher driving force on the active sites of the adsorbent, leading to a higher adsorption capacity (Adebowale et al., 2006). The adsorption capacities of the adsorbents under each initial concentration of Li^+ were as follows: MK-HS>CSK-DMSO>CSK. This can be explained by the changes in the interlayer spacing, specific surface area, and surface activation energy of the modified Kaol. The interlayer spacing of the CSK-DMSO increased after being intercalated, making it easier for the Li^+ to enter the layers and increasing its adsorption performance. The MK-HS experienced higher temperature activation and acid leaching, resulting in more loose microchips and a microtubule accumulation structure, with a better activity and a higher adsorption capacity.

The effect of the contact time on the adsorption of Li^+ was investigated under the same pH and concentration conditions, with contact times ranging from 30 to 180 min (Fig. 5(b)). As the contact time increased, the adsorption

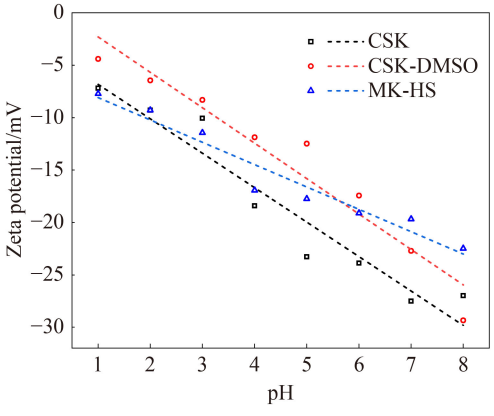

Fig. 4 Zeta potentials of the CSK, CSK-DMSO, and MK-HS at pH values of 1–8.

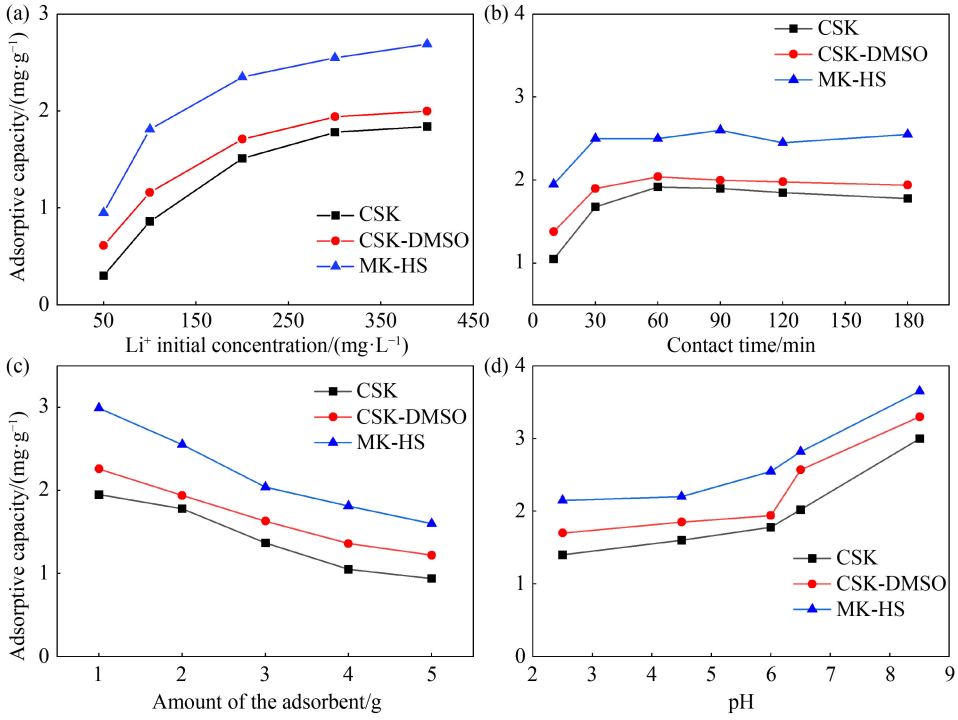

Fig. 5 Effects of the (a) initial concentration, (b) contact time, (c) different doses of adsorbents, and (d) initial pH of hte solution on the adsorption of Li^+ by the CSK, CSK-DMSO, and MK-HS.

effect of the three adsorbents was as follows: MK-HS>CSK-DMSO>CSK. The trends of the adsorption curves are basically the same. The amount of Li^+ adsorption quickly increased to a maximum and then was maintained at a fixed value or slightly decreased. Specifically, the adsorption of the MK-HS reached the maximum value after 90 min; while the adsorption of CSK and CSK-DMSO reached the maximum values after 60 min. The primary amount of adsorption by the three adsorbents exhibited the highest adsorption rate in the first 30 min. This can be explained by the changes in the adsorption active sites on the adsorbents. At the beginning of the adsorption process, a large amount of Li^+ interacted with the adsorption sites, and most of active sites were occupied by Li^+ in the first 30 min (Yu et al., 2000). Thereafter, a large number of active sites on the surfaces were occupied, and the Li^+ began to interact with the more obscure adsorption sites in the adsorbent, which reduced the adsorption rate (Jiang et al., 2010). In addition, because of the higher crushing degree and specific surface area, the per unit adsorption capacity of MK-HS was higher. The reason it reached the maximum adsorption value at 90 min may be that the irregular crushed form blocked the particles, which resulted in some of the active sites not being exposed. A period of oscillation is required to disperse the particles and expose the active sites so that they can interact with the Li^+. The adsorption rates of CSK and CSK-DMSO were basically the same; however, the per unit adsorption capacity of CSK-DMSO was higher. This may be because the extended layer spacing makes it easier for the Li^+ to enter. After reaching the highest amount of adsorption, the amount of adsorption decreased slightly, which may be due to the desorption of Li^+ from the adsorbent. Thereafter, when the adsorption and desorption are consistent, the adsorption process reaches equilibrium.

Figure 5(c) shows the effects of the different dosages of adsorbents on the adsorption of Li^+. Because of the larger specific surface area and interlayer area of MK-HS and CSK-DMSO, respectively, the adsorption effects are still MK-HS>CSK-DMSO>CSK. When the amount of CSK, CSK-DMSO, and MK-HS added was 1 g, the total amounts of adsorption were 1.95 mg/L, 2.26 mg/L, and 2.99 mg/L, respectively. However, when the amount of CSK, CSK-DMSO, and MK-HS added was increased to 5 g, the total amounts of adsorption increased to 4.7 mg/L, 6.1 mg/L, and 8 mg/L, respectively. Although the total amount of Li^+ adsorbed by these three adsorbents increased, the per unit amount of Li^+ adsorption decreased as the adsorbent dosage increased, which indicates that the increase in the solid–liquid ratio reduced the per unit adsorption capacity (He et al., 2019). A high amount of adsorbent may make it difficult for the adsorbent to disperse in the solution. In this situation, the adsorption reaction mainly occurs in the lower part of the container, which may lead to aggregation of some particles and the inability of the adsorbant to fully come in contact with the Li^+ in the solution (Li et al., 2017).

The change in the pH of the solution may affect the interaction between the ions and charges, it will have a

large impact on the process and the results of the adsorption (Zhang et al., 2021). The effect of the initial pH of the solution on the adsorption of Li^+ by the three different adsorbents are shown in Fig. 5(d). When the pH of the three adsorbents and MK-HS was increased from 2.5 to 8.5, the Li^+ adsorption capacity increased simultaneously. Combined with the zeta potential analysis of the three adsorbents, when the pH of the solution was increased from 2.5 to 8.5, the negative charge of the surfaces of these three adsorbents increased, and their capacity to attract cations increased more efficiently, producing a better adsorption effect. Under the same pH conditions, the adsorption properties of the three adsorbents were still MK-HS > CSK-DMSO > CSK, which indicates that the pH of the solution affects the adsorption ability of the adsorbents, but the overall adsorption ability needs to be considered in combination with a variety of factors.

3.5 Adsorption dynamics

As shown in Fig. 6 and Table 3, the fitting results show that the linear correlation coefficients of CSK, CSK-DMSO, and MK-HS data fitted using the pseudo-first-order dynamics model are 0.99437, 0.99773, and 0.99718, respectively, which are slightly higher than the correlation coefficients of the data fitted using the pseudo-second-order dynamic model. This may indicate that the adsorption dynamics in this study conformed to the pseudo-first-order dynamics model. Some important parameters, including the CSK, CSK-DMSO, and MK-HS adsorption rate constants k_{ad} (0.08227, 0.1177, and 0.14792 per min, respectively), were obtained via fitting using pseudo-first-order dynamics models. In addition, the equilibrium adsorption Q_e (theor) values of these adsorbents were 1.86146, 1.98505, and 2.52596 mg/g, respectively, which correspond to the experimental value Q_e (exp). However, although the fitting result of the pseudo-first-order dynamics model is better, the fact that there is little difference between the fitting result of pseudo-second-order dynamics model and pseudo-first-order dynamics model cannot be ignored, especially the fitting results of the MH-HS. This may indicate that most of the adsorption methods are physical adsorption, but there is also the possibility of chemical adsorption (Zhang et al., 2021).

The stick models and the possible Li^+ adsorption mechanisms of CSK, CSK-DMSO, and MK-HS are shown in Fig. 7. Although the specific adsorption form of Li^+ cannot be accurately observed, the following speculation can be made based on the adsorption results, characterization, and adsorption kinetics simulations. In this adsorption experiment, the adsorption of Li^+ led to the complexation of the inner sphere (chemical adsorption) and the outer sphere (physical adsorption). First, physical adsorption is the main adsorption method for CSK. Its relatively stable structure prevented the Li^+ from easily entering the interlayers and the inside of the CSK structure. After the Li^+ came in contact with the CSK, it quickly interacted with the active sites on the surface. However, after intercalation, the DMSO macromolecules were inserted into the interlayers, which

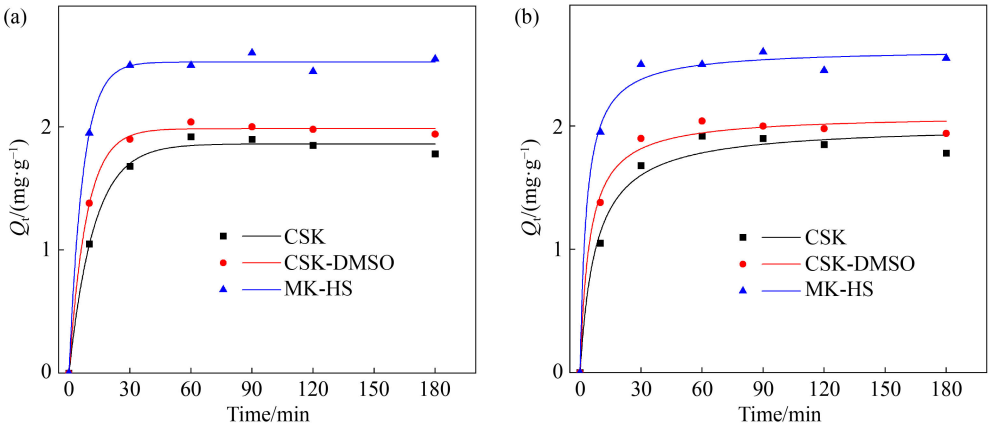

Fig. 6 (a) Pseudo-first-order and (b) pseudo-second-order dynamics models of Li^+ adsorption on the CSK, CSK-DMSO, and MK-HS.

Table 3 Kinetic parameters for Li^+ adsorption at different adsorbents

Adsorbent	Q_e(exp)/(mg·g^{-1})	Pseudo-first-order			Pseudo-second-order		
		k_{ad}/(min^{-1})	Q_e (theor) /(mg·g^{-1})	R^2	k/(g·mg^{-1}·min^{-1})	Q_e (theor) /(mg·g^{-1})	R^2
CSK	1.87	0.08227	1.86146	0.99437	0.0652	2.00917	0.97661
CSK-DMSO	1.99	0.1177	1.98505	0.99773	0.10555	2.09078	0.98882
MK-HS	2.55	0.14792	2.52596	0.99718	0.12247	2.62488	0.99229

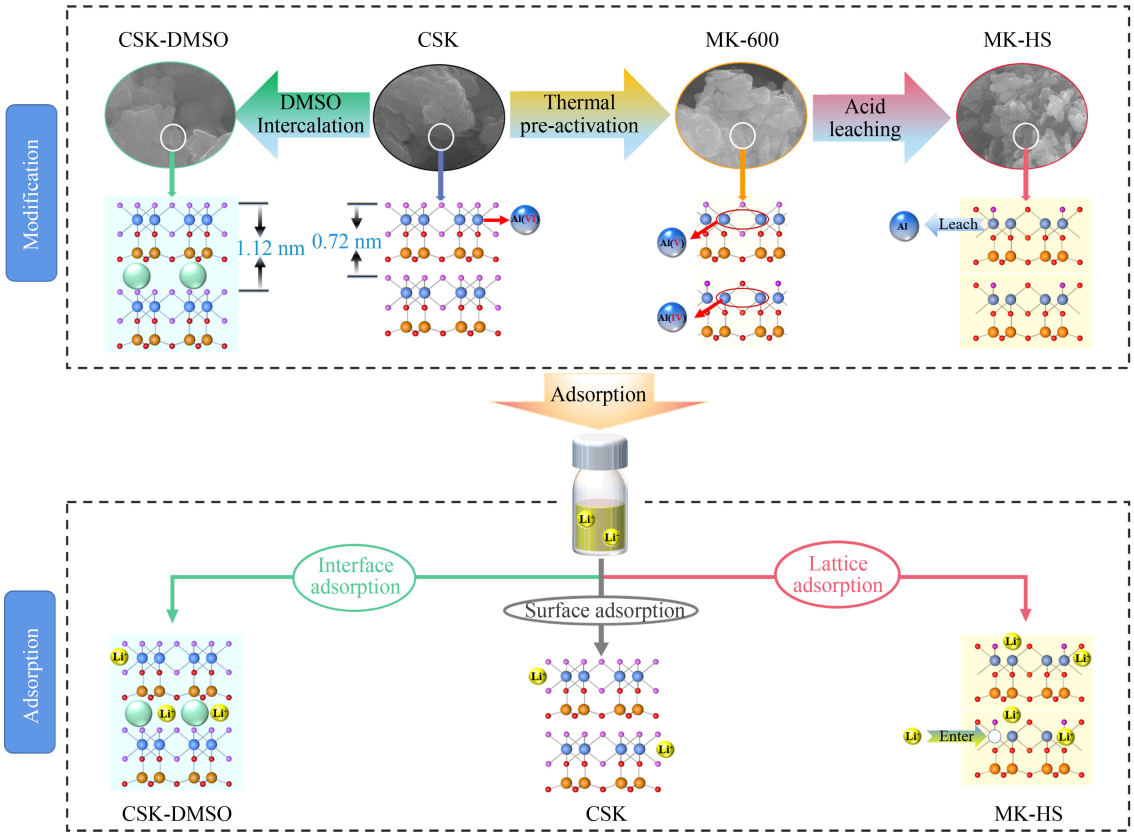

Fig. 7 Stick models and possible Li^+ adsorption mechanisms for the CSK, CSK-DMSO, and MK-HS.

extended the interlayer area and increased the size of the mesoporous, creating good conditions for Li^+ to enter the interlayers. The adsorption was still mainly physical adsorption and adsorption onto the surfaces. Therefore, although the adsorption capacity of CSK-DMSO was improved, it was limited and unstable. In addition, thermal pre-activation and acid leaching seriously damaged the structure of the CSK. The high temperature led to hydroxyl separation and changes in the coordination bonds of the Al, and a large number of microporous structures were produced, which greatly improved the specific surface area of the MK-HS. Furthermore, the contact and reaction between the Li^+ and MK-HS were more sufficient, and the physical adsorption capacity of the MK-HS was greatly improved. The addition of acid further leached the unstable Al, which resulted in the absence of cations in the octahedrons, and Li^+ may have filled these openings and occupied the structural defects in the structure of the Kaol (Wimpenny et al., 2015). Therefore, both chemisorption and physical adsorption dominates the adsorption of Li by the MK-HS, and it had the best adsorption performance.

4 Conclusions

As a type of waste associated with coal mine production, CSK and its two modified forms were successful prepared to study their Li adsorption capacities, and they were found to have excellent Li adsorption capacities. The adsorption results revealed that CSK had a good adsorption capacity for Li^+ in solution, and the two types of modification methods effectively improved the adsorption capacity of CSK. The comprehensive adsorption capacity was found to be as follows: MK-HS>CSK-DMSO>CSK. Specifically, the adsorption was completed in 60 min under alkaline conditions (pH = 8.5), a high solution concentration (400 mg/L), and a low dosage (1 g/100 mL). Furthermore, the analysis of the structures and morphologies of the adsorbents confirmed that the DMSO intercalation method effectively expanded the interlayer space of the CSK, which increased the probability of Li^+ entering the interlayers. Thermal pre-activation and acid leaching at 600°C caused dehydroxylation and structural modification of the CSK and changed the Al(VI) in the lattice into Al(IV), resulting in lattice defects. This increased the specific surface area by over ten times compared to that of the CSK and improved the surface activity, providing the new location for Li^+ to enter. In addition, the adsorption kinetic model demonstrates that the adsorption of Li by the three adsorbents included physical adsorption and chemical adsorption. Hence, the results of this study provide a low-cost and highly effective method of further extracting Li from salt-lake brine and a new application for CSK.

Acknowledgments The authors gratefully acknowledge the financial support provided by the National Natural Science Foundation of China (Grant No. 42172043), the Science and Technology Major Projects of Shanxi Province of China (No. 20181101003), the Fundamental Research Funds for the Central Universities (No. 300102299306), and Scientific Innovation Practive Project of Postgraduates of Chang'an University (No. 300103722045). The authors thank LetPub for its linguistic assistance during the preparation of this manuscript.

References

Adebowale K O, Unuabonah I E, Olu-Owolabi B I (2006). The effect of some operating variables on the adsorption of lead and cadmium ions on kaolinite clay. J Hazard Mater, 134(1–3): 130–139

Bhattacharyya K (2008). Kaolinite and montmorillonite as adsorbents for Fe(III), Co(II) and Ni(II) in aqueous medium. Appl Clay Sci, 41(1–2): 1–9

Bhattacharyya K G, Gupta S S (2006). Kaolinite, montmorillonite, and their modified derivatives as adsorbents for removal of Cu(II) from aqueous solution. Separ Purif Tech, 50(3): 388–397

Bulut Y, Tez Z (2007). Removal of heavy metals from aqueous solution by sawdust adsorption. J Environ Sci (China), 19(2): 160–166

Cao Z, Jia Y, Wang Q, Cheng H (2021). High-efficiency photo-Fenton Fe/g-C3N4/kaolinite catalyst for tetracycline hydrochloride degradation. Appl Clay Sci, 212: 106213

Cheng H, Hou X, Liu Q, Li X, Frost R L (2015). New insights into the molecular structure of kaolinite–methanol intercalation complexes. Appl Clay Sci, 109–110: 55–63

Cheng H, Huang Y, Zhu Z, Dong L, Zha J, Yu M (2021a). Enhanced PbCl2 adsorption capacity of modified kaolin in the furnace using a combined method of thermal pre-activation and acid impregnation. Chem Eng J, 414: 128672

Cheng H, Liu Q, Cui X, Zhang Q, Zhang Z, Frost R L (2012a). Mechanism of dehydroxylation temperature decrease and high temperature phase transition of coal-bearing strata kaolinite intercalated by potassium acetate. J Colloid Interface Sci, 376(1): 47–56

Cheng H, Liu Q, Xu P, Hao R (2018). A comparison of molecular structure and de-intercalation kinetics of kaolinite/quaternary ammonium salt and alkylamine intercalation compounds. J Solid State Chem, 268: 36–44

Cheng H, Liu Q, Yang J, Ma S, Frost R L (2012b). The thermal behavior of kaolinite intercalation complexes—a review. Thermochim Acta, 545: 1–13

Cheng H, Liu Q, Zhang J, Yang J, Frost R L (2010). Delamination of kaolinite-potassium acetate intercalates by ball-milling. J Colloid Interface Sci, 348(2): 355–359

Cheng H, Zhou Y, Feng Y, Geng W, Liu Q, Guo W, Jiang L (2017). Electrokinetic energy conversion in self-assembled 2D nanofluidic channels with Janus Nanobuilding Blocks. Adv Mater, 29(23): 1700177

Cheng M, Yao C, Su Y, Liu J, Xu L, Hou S (2021b). Synthesis of membrane-type graphene oxide immobilized manganese dioxide adsorbent and its adsorption behavior for lithium ion. Chemosphere, 279: 130487

Grosjean C, Miranda P H, Perrin M, Poggi P (2012). Assessment of world lithium resources and consequences of their geographic distribution on the expected development of the electric vehicle industry. Renew Sustain Energy Rev, 16(3): 1735–1744

Gupta S S, Bhattacharyya K G (2005). Interaction of metal ions with clays: I. A case study with Pb(II). Appl Clay Sci, 30(3–4): 199–208

Harvianto G R, Kim S H, Ju C S (2016). Solvent extraction and stripping of lithium ion from aqueous solution and its application to seawater. Rare Met, 35(12): 948–953

He K, Zeng G, Chen A, Huang Z, Peng M, Huang T, Chen G (2019). Graphene hybridized polydopamine-kaolin composite as effective adsorbent for methylene blue removal. Compos, Part B Eng, 161: 141–149

Jia X, Cheng H, Zhou Y, Zhang S, Liu Q (2019). Time-efficient preparation and mechanism of methoxy-grafted kaolinite via acid treatment and heating. Appl Clay Sci, 174: 170–177

Jiang M, Jin X, Lu X Q, Chen Z (2010). Adsorption of Pb(II), Cd(II), Ni(II) and Cu(II) onto natural kaolinite clay. Desalination, 252(1–3): 33–39

Li J, Wang J (2019). Comprehensive utilization and environmental risks of coal gangue: a review. J Clean Prod, 239: 117946

Li X, Deng Z, Li J (2017). Extraction of lithium from salt lake brine with kaolinite. Chemical Indus Eng Progress, 36(6): 2057–2063 (in Chinese)

Liu L, Wang D, Liu X, Li J, Dai H, Yan W (2017). The main types, distribution features and present situation of exploration and development for domestic and foreign lithium mine. Geo China, 44(002): 263–278 (in Chinese)

Luo Q, Dong M, Nie G, Liu Z, Wu Z, Li J (2021). Extraction of lithium from salt lake brines by granulated adsorbents. Colloids Surf A Physicochem Eng Asp, 628: 127256

Makó É, Kovács A, Katona R, Kristóf T (2016). Characterization of kaolinite-cetyltrimethylammonium chloride intercalation complex synthesized through eco-friend kaolinite-urea pre-intercalation complex. Colloids Surf A Physicochem Eng Asp, 508: 265–273

Paranthaman M P, Li L, Luo J, Hoke T, Ucar H, Moyer B A, Harrison S (2017). Recovery of Lithium from geothermal brine with Lithium-Aluminum layered double hydroxide chloride sorbents. Environ Sci Technol, 51(22): 13481–13486

Peng H, Cui C, Cai C, Li S and Zhang X (2014). Research on influence of calcination temperature on metakaolin reactivity and its determination. Bull Chinese Ceramic Soc, 33(8): 2078–2084+2094 (in Chinese)

Razmjou A, Asadnia M, Hosseini E, Habibnejad Korayem A, Chen V (2019). Design principles of ion selective nanostructured membranes for the extraction of lithium ions. Nat Commun, 10(1): 5793

Sen Gupta S, Bhattacharyya K G (2008). Immobilization of Pb(II), Cd(II) and Ni(II) ions on kaolinite and montmorillonite surfaces from aqueous medium. J Environ Manage, 87(1): 46–58

Sun Y, Wang Q, Wang Y H, Yun R P, Xiang X (2021). Recent advances in magnesium/lithium separation and lithium extraction technologies from salt lake brine. Separ Purif Tech, 256: 117807

Suraj G, Iyer C, Lalithambika M (1998). Adsorption of cadmium and copper by modified kaolinites. Appl Clay Sci, 13(4): 293–306

Swain B (2016). Separation and purification of lithium by solvent extraction and supported liquid membrane, analysis of their mechanism: a review. J Chem Technol Biotechnol, 91(10): 2549–2562

Tao S, Bi-wan X, Hui-sheng S (2008). The evolution of coal gangue (CG)–calcium hydroxide (CH)–gypsum–H_2O system. Mater Struct, 41(7): 1307–1314

Uddin M K (2017). A review on the adsorption of heavy metals by clay minerals, with special focus on the past decade. Chem Eng J, 308: 438–462

Wang D, Liu Q, Hou D, Zhang S, Guo P, Cheng H (2017). Improved method for preparation of methoxy-modified kaolinite. J Braz Chem Soc, 29(1): 33–37

Wang M Y, Wang X W, Jiang C J, Tao C F (2014). Solvent extraction of molybdenum from acidic leach solution of Ni–Mo ore. Rare Met, 33(1): 107–110

Wang Y, Cheng H, Hu Q, Liu L, Jia L, Gao S, Wang Y (2022). Pore structure heterogeneity of Wufeng-Longmaxi shale, Sichuan Basin, China: evidence from gas physisorption and multifractal geometries. J Petrol Sci Eng, 208: 109313

Wang Y, Liu L, Cheng H (2021b). Gas adsorption characterization of pore structure of organic-rich shale: insights into contribution of organic matter to shale pore network. Nat Resour Res, 30(3): 2377–2395

Wimpenny J, Colla C A, Yu P, Yin Q Z, Rustad J R, Casey W H (2015). Lithium isotope fractionation during uptake by gibbsite. Geochim Cosmochim Acta, 168: 133–150

Xing H, Liu H, Zhang X, Deng H, Hu H, Yao H J F (2019). Enhanced sodium adsorption capacity of kaolinite using a combined method of thermal pre-activation and intercalation-exfoliation: alleviating the problems of slagging and fouling during the combustion of Zhundong coal. Fuel, 239: 312–319

Xu P, Hong J, Xu Z, Xia H, Ni Q Q (2021). Novel aminated graphene quantum dots (GQDs-NH2)-engineered nanofiltration membrane with high Mg^{2+}/Li^{+} separation efficiency. Separ Purif Tech, 258: 118042

Xu X, Chen Y, Wan P, Gasem K, Wang K, He T, Adidharma H, Fan M (2016). Extraction of lithium with functionalized lithium ion-sieves. Prog Mater Sci, 84: 276–313

Zhang X, Saldi G D, Schott J, Bouchez J, Kuessner M, Montouillout V, Henehan M, Gaillardet J (2021). Experimental constraints on Li isotope fractionation during the interaction between kaolinite and seawater. Geochim Cosmochim Acta, 292: 333–347

Zhao Y, Cao Z, Zuh A A, Jia Y, Wang Q, Cheng H (2022). Synthesis of bismuth oxyiodide/kaolinite composite with enhanced photocatalytic activity. J Phys Chem Solids, 161: 110424

Zhao Y, Wu M, Shen P, Uytterhoeven C, Mamrol N, Shen J, Gao C, Van der Bruggen B (2021). Composite anti-scaling membrane made of interpenetrating networks of nanofibers for selective separation of lithium. J Membr Sci, 618: 118668

Zhou Y, Cheng H, Wei C, Zhang Y (2021). Effect of acid activation on structural evolution and surface charge of different derived kaolinites. Appl Clay Sci, 203: 105997

Zhou Y, LaChance A M, Smith A T, Cheng H, Liu Q, Sun L (2019). Strategic design of clay-based multifunctional materials: from natural minerals to nanostructured membranes. Adv Funct Mater, 29(16): 1807611